Materials Advances

ROYAL SOCIETY OF CHEMISTRY

PAPER

View Article Online
View Journal | View Issue

Cite this: *Mater. Adv.*, 2024, 5, 632

Ginger-derived hierarchical porous carbon as an anode material for potassium-ion batteries and capacitors†

Chandra Sekhar Bongu * and Chandra Shekhar Sharma

Received 19th September 2023,
Accepted 29th November 2023

DOI: 10.1039/d3ma00732d

rsc.li/materials-advances

Carbonaceous materials are ideal as an anode for potassium-ion batteries (KIBs) because of their low cost, tunable physiochemical properties, and excellent reversible intercalation of potassium-ions (K^+). In this work, we propose for the first time an economically viable and environmentally friendly route for producing hierarchical nanoporous activated ginger-derived carbon (AGC). Large interlayer spacing with a disordered microstructure of AGC provides a reason to investigate it as a high-capacity anode for rechargeable KIBs. AGC exhibits excellent electrochemical characteristics under moderate (100 mA g^{-1}) to high rate (1000 mA g^{-1}) discharge conditions. Against a current density of 100 mA g^{-1}, a steady-state reversible capacity of 220 mA h g^{-1} was delivered. Furthermore, a 175 mA h g^{-1} capacity has been demonstrated at a 1000 mA g^{-1} rate for an impressive 1000 cycles. Another striking feature of AGC is its high surface area of 2717 m^2 g^{-1} which makes it a potential candidate as an electrode for constructing a potassium-ion capacitor (KIC). AGC was used as a negative electrode while activated candle soot (ACS) as the positive electrode to develop a dual carbon KIC with high-rate capability. The as developed dual carbon KIC delivered a reversible capacity of 120 mA h g^{-1} over 100 cycles at 50 mA g^{-1}. In essence, due to the extraordinary physiochemical characteristics, AGC is therefore not only a superior electrode material to other biomass-derived carbons but also a viable contender for various other electroactive applications.

1. Introduction

The demand for new, advanced and sustainable batteries with high energy density is growing in response to developing electronic devices, electric cars, and smart grids.[1–3] The current use of lithium-ion batteries in large-scale energy storage applications such as electric vehicles has led to a rapid depletion of available lithium supplies and an increase in costs.[4–9] As a result, addressing the demand for stationary energy storage at a low cost and with the fewest rare components possible has become critical. The scientific community has been focusing on sodium-ion batteries for the past decade or so, due to the abundance of sodium and the "rocking chair" electrochemical behavior similar to LIBs.[10] However, due to recent advancements in anode and cathode materials for potassium-ion batteries, as well as whole-cell prototypes, the state of this emerging field is rapidly evolving. Potassium-ion batteries may have many advantages compared to sodium-ion batteries. According to reports, the redox potential of potassium is lower than that of sodium (standard electrode potentials are −2.93, −2.71 *vs.* the standard hydrogen electrode, respectively), implying that high voltage and high energy density batteries are similar to lithium-ion batteries (lithium redox potential of −3.04 V *vs.* SHE).[11] When compared to lithium, potassium is a more abundant element on the planet, accounting for 1.5% *vs.* 0.0017% for Li, and its cost is around one-tenth that of lithium.[12] Although the higher radius of the K ion (0.138 nm *vs.* 0.102 nm (Na ion) and 0.076 nm (lithium-ion)) may obstruct the intercalation process, its compatibility with some electrolytes, such as 1,2-dimethoxyethane (DME) has been demonstrated to produce an even smaller K ion-solvent Stroke's radius, which may have kinetic benefits.[13]

According to previous studies, non-carbon anodes have several disadvantages that are difficult to overcome. Metal anodes, for example, have a mainly reversible alloying reaction with K, although the alloy produces a significant volume change.[14–16] Carbon materials have emerged as the most viable solution for KIBs among all anode materials when considering economic efficiency, environmental friendliness, sustainability, outstanding electrolyte accessibility, and adjustable interlayer

Creative & Advanced Research Based on Nanomaterials (CARBON) Laboratory, Department of Chemical Engineering, Indian Institute of Technology Hyderabad, Kandi-502285, Telangana, India. E-mail: chandrasekharbongu@gmail.com

† Electronic supplementary information (ESI) available. See DOI: https://doi.org/10.1039/d3ma00732d

space.[17–21] As a result, various carbon-based materials have been investigated for KIBs, such as carbon fiber, graphite, hard carbon, soft carbon, activated carbon, and composite materials to see if they may increase the K-ion storage capability of KIBs.[11,17,22–29]

Recently, the synthesis of porous and disordered carbon materials from bio-waste has gained significant importance based on the bio-waste-derived carbons that find various applications because of their abundant availability and low cost.[7,30–40] The development of full KIBs from biowaste-derived materials will not only lower the cost of raw materials, resulting in lower production costs, but will also create a sustainable and clean environment.[41] For example, Qing *et al.* successfully prepared a carbon material using corn husk and used it as an anode for KIBs.[42] Lotfabad *et al.* generated hard carbon from biomass *via* pyrolysis of banana peels, and this hard carbon demonstrated good electrochemical performance.[43] Zhenrui Wu and co-workers reported the carbon obtained from loofah as an anode material with the capacity of 150 mA h g^{-1} at 100 mA g^{-1} over 200 cycles.[44]

Inspired by the above developments, herein, we demonstrate ginger as a novel, low-cost, and easily available precursor for the synthesis of unique interconnected hierarchical porous carbon nanosheets. In addition to domestic garbage at home, we gather waste ginger from the locals in the southern region of India, particularly after making ginger tea, which discards significant amounts of ginger. This waste material, which was deemed unsuitable for any other use, was gathered and processed in an effort to convert it from filth to wealth. It was then used as an electromagnetic composite by biomass transmission and an electrode material for KIBs.[45–49] The high surface area and interconnected porous character of carbon as derived from ginger have resulted from KOH activation during carbonization. The in-house produced interconnected porous carbon facilitates large accessible surface-active sites for electrolyte interaction and has been demonstrated as a potential anode for KIBs through this study for the first time. In other words, ginger-derived carbon material has an outstanding capacity of 380, 250, and 175 mA h g^{-1}, corresponding to current densities of 100, 500, and 1000 mA g^{-1}, respectively. Specifically, in-house synthesized carbon exhibits high reversible capacity and ultralong life. Furthermore, we successfully developed a low-cost asymmetric potassium dual carbon capacitor, which was constructed with activated ginger carbon (AGC) as an anode and activated candle soot carbon (ACS) as the cathode. This research aids in the development of a biomass derived carbon as a promising KIB anode material.

2. Experimental details

2.1. Material synthesis

Synthesis of AGC involves a simple approach as described below and shown in a schematic as Fig. 1. The ginger was collected from the local market, washed thoroughly with water, cut into small pieces, and dried subsequently at 80 °C for 24 h. Pre-carbonization was carried out at 400 °C under a nitrogen atmosphere for 3 h. Afterward, the pre-carbonized material was mixed with KOH in a 1 : 3 ratio, and the furnace heated at 800 °C for 2 h with a heating rate of 5 °C min^{-1} in a nitrogen atmosphere. The powder thus obtained was washed thoroughly with 1 M HCl to remove metal impurities and washed repeatedly with distilled water until it attains a neutral pH. The resulting carbon material was dried at 100 °C. The synthesized carbon material is denoted as AGC.

2.2. Activated candle soot carbon (ACS)

As per our previous report, candle soot carbon was prepared as below.[50] On a steel plate, burning candle soot was gathered

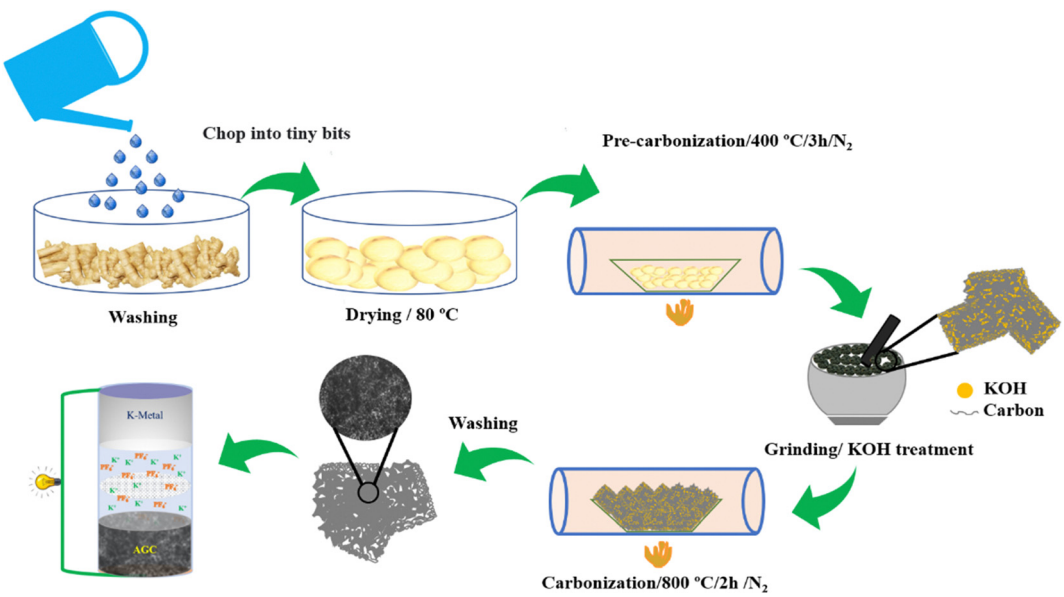

Fig. 1 Schematic illustration of the preparation of activated ginger-derived carbon.

from the flames tip and cleansed using ultrasonic technology to get rid of the impurities. The accumulated soot was scraped off the surface and heated to 450 °C for two hours in an air environment. To activate the candle soot carbon, it was soaked in KOH solution in the mass ratio of 1 : 3 and then the furnace was heated at 700 °C for 2 h with a heating rate of 5 °C min^{-1} in a nitrogen atmosphere. The powder thus obtained was washed thoroughly with 1 M HCl to remove metal impurities and washed repeatedly with distilled water until it attains a neutral pH and dried at 100 °C.

2.3. Material characterization

X-ray diffraction (PANalytica X'pert pro-X-ray diffractometer) of the sample was recorded with a Cu-Kα radiation (λ = 1.5406 Å) source. Raman spectra (WITec Raman spectroscopy) were obtained by using green laser excitation (λ = 532 nm with excitation energy of 2.33 eV). Field emission scanning electron microscopy (FESEM) images of the samples were captured using a JEOL-JEM-2011(200KV) system, and transmission electron microscopy (TEM) images of the samples were obtained using a JEOL-JSM-700F. The specific surface area and pore size distribution of the product were determined by using N_2 adsorption isotherms (Autosorb iQ, Quantachrome, USA).

2.4. Electrochemical measurements

Electrochemical measurements were carried out using CR2032 type coin cells, wherein copper foil has been used as the current collector, potassium metal as both the counter electrode and reference electrode, and glass microfiber as the separator. The electrolyte of 0.8 M of KPF_6 in a 1 : 1 (v/v) mixture of ethylene carbonate (EC) and dimethyl carbonate (DMC) was prepared and stored in an Ar-filled glovebox. To make a working electrode, a slurry was prepared by mixing ginger carbon (activated and inactivated) (70 wt%) as the active material, Super-P as a conductive carbon (20 wt%), and polyvinylidene fluoride binder (10 wt%) in *N*-methyl-2-pyrrolidone as solvent. The slurry was coated on copper foil and dried in an oven at 80 °C to evaporate NMP. The hot roll is pressed to ensure better adherence and cut into circular discs of 1 mm diameter to act as an anode in the coin cell assembly. The coin cell (CR2032) was assembled in a high-purity Ar-filled glovebox with water and oxygen content lower than 1 ppm. Cyclic voltammetry (CV) was recorded on a VMP3 multichannel potentiostat–galvanostat system (Biologic Science Instrument) in the potential window of 0.01–3.0 V and at the scan rate of 0.05 mV s^{-1}. Before the manufacturing of the full KIC cell, the AGC anode was prepotassiated utilizing the half-cell configuration at 50 mA g^{-1}. The loading of the cathode material and anode material was about 1 mg and 0.3 mg, respectively, which was cycled within 0.01 to 3.5 V. The charge–discharge behaviour was investigated using a biological battery cycler. Electrochemical impedance spectroscopy (EIS) measurements were carried out using a biologic VSP electrochemical workstation in the frequency range from 10 KHz to 100 mHz with an amplitude voltage of 10 mV at room temperature.

The energy density (E) and power density (P) of the supercapacitor cell were estimated according to eqn (1) and (2), respectively, represented as:

$$E = \frac{0.5 C_{CD}(V_f - V_i)^2}{3.6} \quad (1)$$

$$P = \frac{3600E}{\Delta t} \quad (2)$$

where C_{CD} (F g^{-1}) signifies the specific capacitance, $(V_f - V_i)$ (V) represents the potential window, and Δt (t) is the discharge time from the charge–discharge curve in the case of the device.

3. Results and discussion

3.1. Physiochemical characterization

The structural characterization of AGC has been carried out by powder X-ray diffraction study, as shown in Fig. 2a. We can observe two peaks at 2θ = 23.4° and 43.4°, which can be assigned to the (002) and (100) crystallographic planes of graphite, respectively, and the wide and broad peaks reflect the amorphous characteristic of the AGC material.[51] The (002) plane computed d spacing value is 0.386 nm higher than the

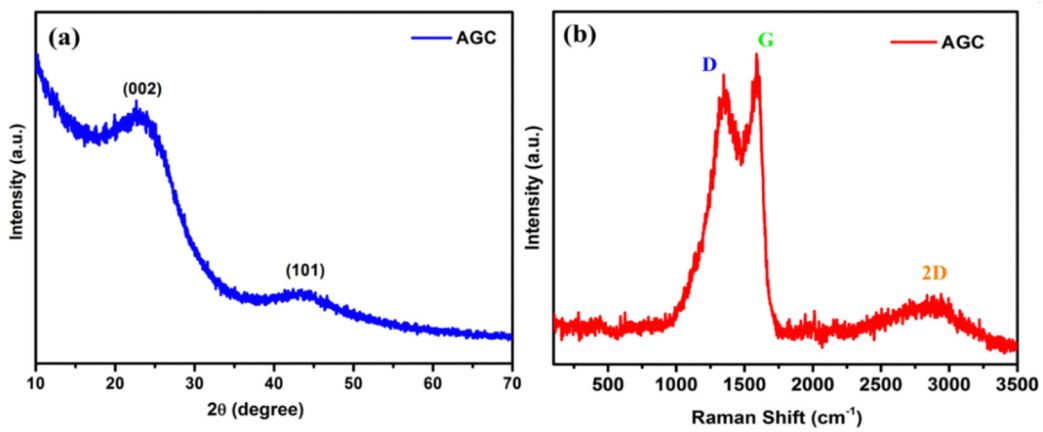

Fig. 2 (a) XRD pattern and (b) Raman spectrum of AGC.

pure graphitic carbon structure (0.335 nm). The large interlayer spacing allows for the de/intercalation of potassium ions between the layers.[52] The peak at 2θ = 43.4° with a lower intensity results from the (001) plane due to the low graphitic character of the as-prepared AGC sample. According to the XRD results, the carbon produced from ginger has a significant quantity of the amorphous phase combined with the low graphitic form.

The papered carbon (AGC) sample was subjected to Raman spectroscopy analysis to establish its graphitic and amorphous structure, as shown in Fig. 2b. In the Raman spectra, two main peaks were exhibited at around 1350 cm^{-1} and 1587 cm^{-1} corresponding to the disordered D band (defect band, corresponding to the A_{1g} vibration mode) and graphitic G band (graphite band, corresponding to the E_{2g} hexagonal graphitic lattice), respectively.[53] The D-band is related to the sp^3-bond of defective carbon structures, and the G-band represents the conjugated structure of the sp^2-bond of graphitic carbon domains. The number of structural flaws and the level of molecular order inside the carbon structure can be expressed by the intensity ratio of the D-band and G-band (I_D/I_G). The I_D/I_G ratio of AGC was 0.96, which confirms the highly disordered structure of the synthesized carbon.[42] Furthermore, a minor hump with a maximum at 2876 cm^{-1} is a typical peak of two-dimensional (2D) materials, indicating the presence of additional stacked graphite-like layers in AGC and the high degree of order of the graphitic layers with pseudo-graphite units.[44] As a result, AGC with a lot of interlayer space and a lot of disordering may be an ideal material for storing and releasing K ions.

Nitrogen adsorption–desorption measurements were used to evaluate the specific surface area and porosity of the carbon produced from ginger (Fig. 3a and b). The adsorption isotherm has Type II features, showing that the carbon is microporous with mesoporosity, implying a complex pore structure and network effect in the sample. The large presence of micropores in the carbons is revealed by the adsorbed nitrogen in the initial relative pressure range (less than 0.1). Furthermore, the presence of well-developed mesopores is suggested by the detected hysteresis loops in the relative pressure range of 0.4 to 0.9.[54–56] As shown in Fig. 3b, the majority of the micropores in the sample are bigger than 1.7 nm. Therefore, the sample possesses both micro and mesopores. Furthermore, the Brunauer–Emmett–Teller (BET) specific surface area (SSA) of the AGC was measured to be 2717 $m^2\ g^{-1}$, whereas the micropore surface area was 1621 $m^2\ g^{-1}$. The interconnected micro and mesopores can efficiently shorten the ion diffusion distance, and the pore walls can act as highways for electron transport, boosting the rate performance and cycling stability. As a result, the large SSA and hierarchical interconnected porous structure can ensure adequate contact between the electrolyte and the active material surface, resulting in offering a well-organized path for ion transport.[57,58] Therefore, AGC with micro and mesopores, high interlayer spacing, and disordered microstructure possesses all characteristics needed for storing and releasing K ions.

To further understand the surface features of the AGC material, X-ray photoelectron spectroscopy (XPS) was used to analyze the chemical composition, as shown in Fig. 4. The AGC is mostly constituted of C and O, as demonstrated in the XPS survey spectrum (Fig. 4a), with atomic concentrations of 90.4 and 9.6%, respectively. The high resolution deconvoluted C 1s spectrum (Fig. 4b) shows four peaks at about 282.1, 284.8, 286.6, and 288.5 eV, corresponding to the C–C/C═C, C–OH, C═O, and COOH bonds, respectively (Table 2). The high-resolution XPS spectrum of O 1s (Fig. 4c) can be deconvoluted into three peaks at binding energies of 530.6, 531.6, and 533.1 that are ascribed to O–I (C═O carbonyl groups), O–II (C–OH hydroxylic groups or C–O–C ether groups), and O-III (COOH carboxyl groups) (Table 1).[51,59] The individual atomic percentages of C═O, C–OH or C–O–C, and COOH are 34.1%, 33.9%, and 32.0%, respectively. Although the presence of oxygen atoms in the carbon framework may diminish the materials' electroconductivity, on the other hand, it can improve the wettability by reducing the inert surface area and providing several active sites.[59] To be more specific, the C–OH hydroxyl groups promote carbon material wetting, while the presence of C═O in carboxyl groups can boost surface acidity.

Fig. 5 shows the SEM and TEM images for the as-prepared activated ginger carbon materials. SEM images of AGC are

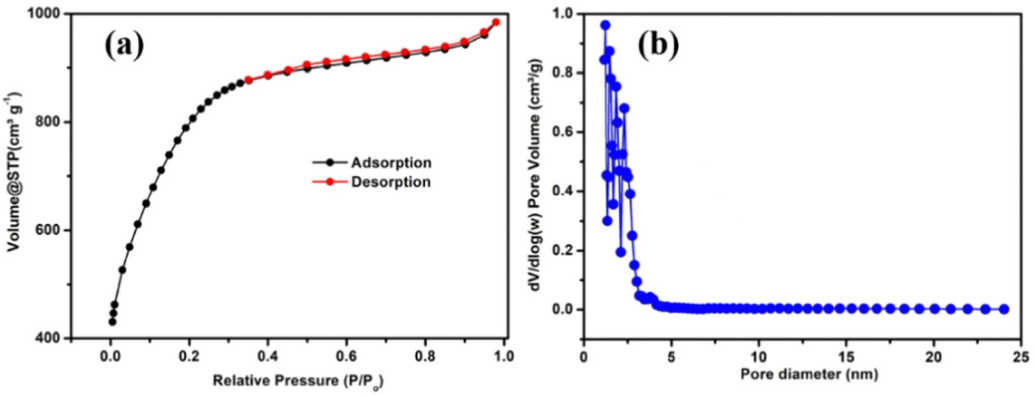

Fig. 3 (a) Nitrogen adsorption–desorption isotherm, and (b) pore size distribution of AGC.

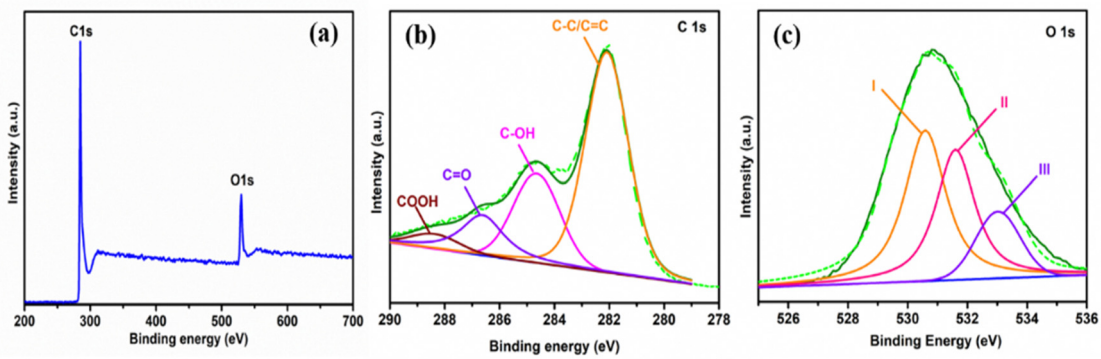

Fig. 4 (a) XPS survey spectrum. High-resolution XPS spectra for (b) C 1s and (c) O 1s.

Table 1 Peak assignment of C 1s and O 1s of the synthesized AGC

Peak	Binding energy (eV)	Assignment	Atom %
C 1s	282.1	C–C/C═C	91.0
	284.8	C–OH	
	286.6	C═O	
	288.5	COOH	
O 1s	530.6	C═O	9.0
	531.6	–C–OH/C–O–C	
	533.1	COOH	

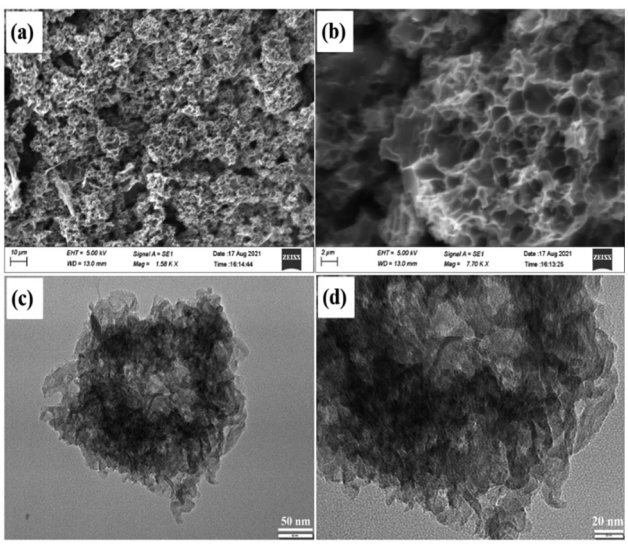

Fig. 5 (a and b) SEM and (c and d) TEM images of the AGC.

shown in Fig. 5a and b, demonstrating the densely linked hierarchically porous structure. These uniformly distributed pores of AGC possibly arise when the pre-carbonized char of ginger was activated with KOH.[60] The more detailed texture of the AGC material was examined with TEM images (Fig. 5c and d) and high-resolution TEM images (Fig. S1, ESI†). Fig. S1 (ESI†) shows graphitization interlayer spacing in the AGC. As seen in Fig. 5c, the carbon structure contains graphene-like wrinkled nanosheets that are intertangled and well-connected, resulting in a highly porous carbon network. The presence of a unique porous structure can improve the K-ion transport and reduce the internal resistance of the material as discussed in the next section.

3.2. Electrochemical characterization

We employed a 2032 button battery for half-cell configuration, and AGC was used as the anode material and the electrochemical performance was tested. The electrochemical K ion storage properties of AGC were investigated using CV and EIS. Fig. 6a exhibits the first five CV profiles of the AGC anode in the potential range of 0.01 to 3.00 V at a scan rate of 0.05 mV s^{-1}. In the first cycle, the cathodic peak appears at 0.71 V, which demonstrates electrolyte decomposition and the formation of a solid electrolyte interphase (SEI) layer, which is primarily responsible for the irreversible capacity during the first discharging/charging cycle.[61–63] The cathodic peak disappeared from the subsequent cycles, ensuring the stable SEI formation and the cycling stability of the electrode.[64] Another strong peak around 0.5 V corresponds to the intercalation of K ions into the AGC layers and the KC_8 formation.[11,21,65] The deintercalation of K ions from AGC is represented by the wide anode peak from 0.2 to 0.5 V.[66] Furthermore, most of the CV curves overlap after the second cycle, indicating strong reversibility of the potassium ion insertion/de-insertion processes in the AGC electrode.

The selected charge–discharge curves of the AGC anode at a current density of 100 mA g^{-1} are shown in Fig. 6b. The AGC sample initial charge/discharge curves follow the same pattern as the CV curves, indicating highly reversible K-ion storage. The first cycle discharge/charge capacities of the AGC anode are 650 and 401 mA h g^{-1}, respectively, greatly exceeding the theoretical capacity of graphite, which is 272 mA h g^{-1} and corresponding to an initial coulombic efficiency (ICE) of 61.7%. The SEI layer creation on the AGC surface can be linked to the low Coulombic efficiency, which can also be seen in the CV result.[65] The coulombic efficiency of the AGC electrode increases slowly in the subsequent cycles and remains lower than 90% until the 10th cycle (Fig. 6c) due to the hierarchical porous structure and large specific surface area. The low initial efficiency and slow capacity stabilization requiring a longer time for the SEI layer to

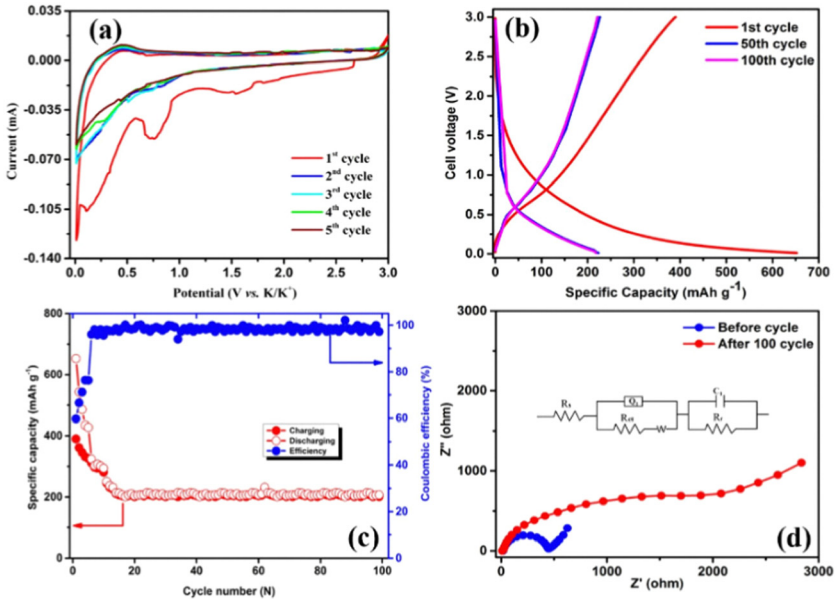

Fig. 6 (a) Cyclic voltammogram of the synthesized AGC anode cycled between 0.1 and 3.0 V *vs.* K^+/K with the scan rate of 0.05 mV s^{-1}. (b) Discharge–charge profiles of the AGC anode at 100 mA g^{-1}. (c) Cycling stability and coulombic efficiency of the AGC anode at the current density of 100 mA g^{-1}. (d) EIS spectra of the as-fabricated AGC anode (blue color) and the cell under the influence of 100 mA g^{-1} after 100 cycles (red color) and the fitted equivalent circuit.

form fully is a frequent phenomenon in porous carbon materials. As a result, at 100 mA g^{-1}, a steady-state reversible capacity of 220 mA h g^{-1} (100 cycles) and the coulombic efficiency of 99% was attained (Fig. 6c) after 20 cycles, which is higher than that of previous other biomass-derived carbons (Table 3).[42,44,67–72] These phenomena prove that the existence of a large number of micro and mesopores in AGC is responsible for the high specific capacity reported, as they operate as a potassium reservoir, favoring the transit path and increasing K ion diffusion and electrolyte penetration.

To further demonstrate the storage mechanism of K ions in AGC, the CV curves were recorded at various scan rates ranging from 0.1 to 1 mV s^{-1} and the *b* value was calculated (Fig. S2, ESI†). The power-law formula $I = a\nu^b$ describes the peak current *I* and scan rates (ν), where *a* and *b* are constants. Plotting the current and sweep rate in the logarithm $\log i = b \log \nu + \log a$ yields the *b*-value. The current is contributed by capacitive behavior (surface-induced K storage) when the *b*-value is 1, and the current is dominated by the ion-diffusion regulated contribution when the *b*-value is 0.5 (intercalating K storage).[73] The *b*-value might range from 0.5 to 1, indicating the presence of mixed processes in the charge storage process. The *b*-value calculated for AGC (0.73) from the CV curves (slope of $\log i$ *vs.* $\log \nu$) and shown in Fig. S2b (ESI†) indicates that the capacitive process is dominated and the diffusion process also exists in the charge storage process. The cathodic peak suggests that AGC exhibits a diffusion-controlled charge storage mechanism. To understand quantitatively, the percentage contributions of the diffusion-controlled process and capacitive process of the AGC electrode were determined using Trasatti method analysis and the relevant graphs are shown in Fig. S3a–c (ESI†), where a full explanation of the Trasatti analysis method is also provided. Fig. S3c (ESI†) shows a bar plot of the AGC electrode material's specific capacity with diffusion-controlled and capacitance contributions. AGC has an 81% diffusion-controlled and 19% capacitance-controlled contribution due to the K ions stored in the carbon inter-layer spacing and the shortened ion diffusion path. To have a better understanding of the capacity decay and diffusion kinetics change of the AGC under the current density of 100 mA g^{-1}, EIS is conducted with a frequency range from 10 kHz to 100 mHz. From the EIS (Fig. 6d), there is not much change of electrolyte resistance before and after discharge/charge. However, the decrease in the Warburg type impedance slope indicates that the electron transfer inside the battery becomes more difficult with the accumulation of the SEI layer on the surface during cycling. The fitted equivalent circuit was in Fig. 6d. From the circuit, the electron transfer resistance (R_{ct}) change was very much in the high-frequency region, and before and after the 100 cycles, it was 440 to 2500 Ω (Table 2). Furthermore, such a large rise could be attributed to a rapid loss of electrochemical active sites, or it could be owing to a massive volume change expansion and irreversible potassium accumulation.[74,75]

The rate performance of AGC is evaluated in Fig. 7a. It also exhibits the best rate performance, delivering reversible capacities of 576, 431, 365, 340, 286, 180, and 240 mA h g^{-1} at 20, 40, 80, 100, 500, 1000, and 100 mA g^{-1}, respectively. When

Table 2 Variation of impedance of the AGC anode under the influence of 100 mA g^{-1} current density

S. no.	Before cycling	After 100 cycles
R_s	16.9	10.4
R_{ct}	440.0	2500.0

Table 3 Performance of the biomass-derived carbon material as KIB anodes

Anode materials	Electrolyte	Current density	Reversible capacity (mA h g^{-1})	Ref.
Potato	KFSI in DME	500 mA g^{-1}	207	66
Corn husk	0.8 M KPF_6 in EC:DEC	2 A g^{-1}	167	42
Loofah-derive carbon	1 M KPF_6 in EC:DEC	100 mA g^{-1}	100 (400th cycle)	44
Walnut septum	0.8 M KPF_6 in EC:DEC	1 A g^{-1}	120 (1000th cycle)	67
Bamboo charcoal	KPF_6 in EC:DEC	200 mA g^{-1}	203 (300th cycle)	68
Maple leaves	1.0 M $KClO_4$ in EC:DEC	500 mA g^{-1}	181	69
Sugar cane	1 M KPF_6 in EC:DEC	2 A g^{-1}	182	70
Cyanobacteria	0.8 M KPF_6 in EC:DEC	500 mA g^{-1}	180	71
Ginger derived carbon	0.8 M KPF_6 in EC:DEC	500 mA g^{-1}	286	This work
		1000 mA g^{-1}	175	

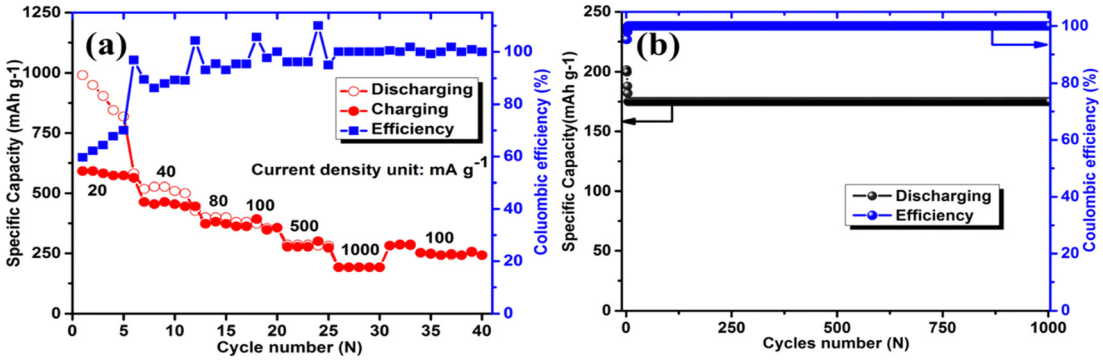

Fig. 7 (a) Rate capability at current densities from 20 to 1000 mA g^{-1} and (b) long-term cycling performance at 1000 mA g^{-1} of AGC.

compared to alternative biomass-derived carbons, the AGC anode exhibits better reversible capacities at higher current densities (500 and 1000 mA g^{-1}).[67–72] More interestingly, after subjecting the cell to varied high current densities, a reversible capacity of 240 mA h g^{-1} was attained, especially when switched back to 100 mA g^{-1}. Fig. 7b shows that AGC has outstanding long-term cycling stability, with a reversible specific capacity of 175 mA h g^{-1} after 1000 cycles at a current density of 1000 mA g^{-1}. To the best of our knowledge, the AGC anode has a higher reversible capacity and rate performance

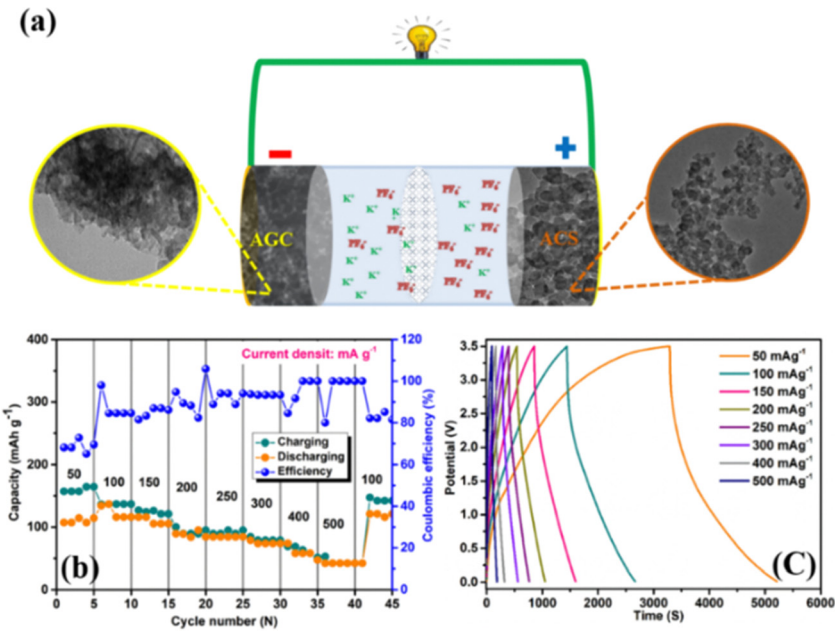

Fig. 8 Electrochemical performance of the AGC//ACS K-ion capacitor: (a) schematic illustration of the fabrication of the KIC full cell, (b) rate capability at current densities from 50 to 500 mA g^{-1}, and (c) GCD curves recorded at different current densities.

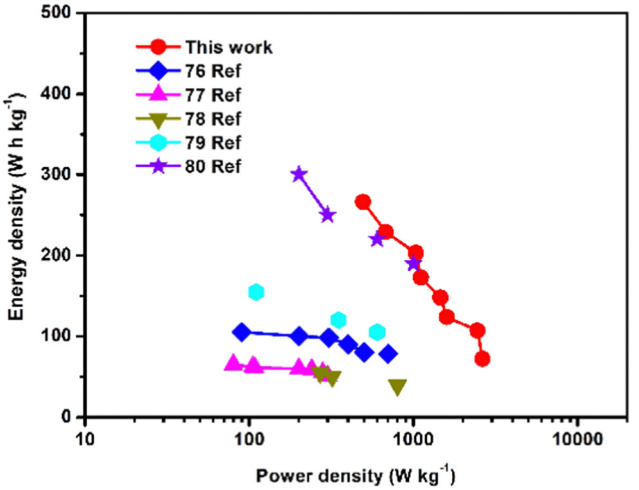

Fig. 9 Ragone plot with specific energy and power density compared with previous KIC devices.

than any other amorphous carbon generated from various biomass sources. As a result, AGC qualifies as a low-cost, high-capacity, high-rate anode material for KIBs, opening new avenues for developing economically feasible and environmentally friendly KIB electrode materials.

3.3. Dual carbon potassium-ion capacitor (KIC)

To investigate the electrochemical properties further, we constructed an asymmetric dual carbon potassium ion capacitor (KIC) using potassiation AGC as the anode, activated candle soot carbon (ACS) as the cathode, and KPF_6 containing organic electrolyte (Fig. 8a). In the charging process, when PF_6^- ions are absorbed in the ACS and K^+ are intercalated in AGC, the discharge process is completely reversible. The asymmetric KIC has two types of electrode material in the positive and negative electrodes, which work in various electrochemical potential windows and have different specific capacities. Before fabricating the full cell, the half-cell was fabricated with ACS and the CV, cycling study and charge discharge profiles were carried out, and presented in Fig. S4 (ESI†). At a current density of 100 mA g^{-1}, the specific capacity of AGC and ACS in their designated working potential windows is around 300 mA h g^{-1} and 75 mA h g^{-1} (Fig. S4b, ESI†), respectively. As a result, the optimal mass ratio of the two electrodes should be 3.8 to 4 and the voltage window 0.01 to 3.5 V (Fig. S5, ESI†). The charge/discharge performance of the dual carbon KIC was investigated at various current densities (Fig. 8b), yielding the revisable capacities of 164, 136, 121, 94, 84, 78, 51 and 42 mA h g^{-1} at 50, 100, 200, 250, 300, 400 and 500 mA g^{-1} current densities, respectively. Moreover, the revisable capacity recovered to 147 mA h g^{-1} at 100 mA g^{-1} current density even after high current density was applied to the ACS//AGC. The decrease in the device capacity at high current densities due to the accessibility of the electrochemical active sites being lower. Fig. 8c displays the GCD curves of the ACS//AGC device in the shape of quasilinear, indicating that the carbon materials combined capacitor-type and battery-type charge storage behavior.[76] Furthermore, as shown in Fig. S3 (ESI†), the KIC shows a reversible capacity of 120 mA h g^{-1} over 100 cycles at 50 mA g^{-1}. Notably, a rise in the capacitance from the 20th cycle onwards is due to the oxygen functional groups and activation of the electrode material. The half-cell and full-cell show outstanding results due to the rapid ion transport, which is provided by a high specific surface area and rich porous architectures of nanocarbon derived from AGC through a potential channel pathway.

Fig. 9 Ragone plot contrasts our AGC//ACS KIC device with those of other hybrid capacitors. Our created device has a high energy density and power density since it uses carbons made from activated candle soot and activated ginger (calculated from eqn (1) and (2)). Comparing our designed KIC to other documented devices as AS-HC//AS-AC, N-CNTs//LCG, NGC//$K_2Ti_6O_{13}$, K-V_2C, and MHC//ACF, we find that they exhibit higher energy and power densities.[76–80] These remarkable results are explained by the quick ion transport provided by the high specific surface area of carbons produced from activated ginger and activated candle soot *via* a possible channel mechanism.

4. Conclusions

In conclusion, porous carbon material was successfully synthesized using a simple activation method, with low-cost ginger as the precursor and KOH as the activating agent. Activated carbon as derived from ginger (AGC) with an interlayer spacing of 0.38 nm and interconnecting micro and mesopores with a high BET surface area of 2717 m^2 g^{-1} can alter the electrical structure, increase conductivity, and improve wettability, resulting in improved electrochemical performance. When the obtained AGC is applied as the anode in KIBs, it exhibits superior electrochemical performance under both conventional and high-rate. At 100 and 1000 mA g^{-1}, it produces a steady-state reversible capacity of 220 and 175 mA h g^{-1}. The combination of micro and mesoporous carbon having interconnected graphene sheets and a high surface area may explain the AGC anodes improved electrochemical performance over other biomass-derived carbons. To the best of our knowledge, this is the first report that shows the anode behavior of ginger-derived carbon material for use in potassium-ion batteries. We also demonstrated the use of AGC along with ACS for the dual carbon K-ion capacitor. The low-cost, simple, and controllable synthesis technique should result in large-scale industrial production of AGC to address the demand for long-term energy storage.

Conflicts of interest

There are no conflicts to declare.

References

1 M. Armand and J.-M. Tarascon, *Nature*, 2008, **451**, 652–657.

2 C. Wei, H. Fei, Y. An, Y. Zhang and J. Feng, *Electrochim. Acta*, 2019, **309**, 362–370.
3 Y. Wei, Y. Yan, Y. Zou, M. Shi, Q. Deng, N. Zhao, J. Wang, C. You, R. Yang and Y. Xu, *Electrochim. Acta*, 2019, **310**, 45–57.
4 H. Pan, Y.-S. Hu and L. Chen, *Energy Environ. Sci.*, 2013, **6**, 2338–2360.
5 W. Luo, F. Shen, C. Bommier, H. Zhu, X. Ji and L. Hu, *Acc. Chem. Res.*, 2016, **49**, 231–240.
6 L. Meng, C. Hou, J. Hou, H. Xie, Z. Yue, H. Lu, S. Yang and B. Gong, *Eng. Sci.*, 2022, **20**, 134–143.
7 M. Culebras, G. A. Collins, A. Beaucamp, H. Geaney and M. N. Collins, *Eng. Sci.*, 2022, **17**, 195–203.
8 D. Wang, R. Wang, K. Huang, M. Lei and H. Tang, *Adv. Compos. Hybrid Mater.*, 2022, **5**, 1362–1375.
9 Y. Zhang, L. Liu, L. Zhao, C. Hou, M. Huang, H. Algadi, D. Li, Q. Xia, J. Wang and Z. Zhou, *Adv. Compos. Hybrid Mater.*, 2022, **5**, 2601–2610.
10 Q. Wang, B. Zhao, S. Zhang, X. Gao and C. Deng, *J. Mater. Chem. A*, 2015, **3**, 7732–7740.
11 W. Luo, J. Wan, B. Ozdemir, W. Bao, Y. Chen, J. Dai, H. Lin, Y. Xu, F. Gu and V. Barone, *Nano Lett.*, 2015, **15**, 7671–7677.
12 J. C. Pramudita, D. Sehrawat, D. Goonetilleke and N. Sharma, *Adv. Energy Mater.*, 2017, **7**, 1602911.
13 Y.-H. Zhu, Q. Zhang, X. Yang, E.-Y. Zhao, T. Sun, X.-B. Zhang, S. Wang, X.-Q. Yu, J.-M. Yan and Q. Jiang, *Chem*, 2019, **5**, 168–179.
14 I. Sultana, T. Ramireddy, M. M. Rahman, Y. Chen and A. M. Glushenkov, *Chem. Commun.*, 2016, **52**, 9279–9282.
15 Y. An, Y. Tian, L. Ci, S. Xiong, J. Feng and Y. Qian, *ACS Nano*, 2018, **12**, 12932–12940.
16 I. Sultana, M. M. Rahman, Y. Chen and A. M. Glushenkov, *Adv. Funct. Mater.*, 2018, **28**, 1703857.
17 Z. Jian, Z. Xing, C. Bommier, Z. Li and X. Ji, *Adv. Energy Mater.*, 2016, **6**, 1501874.
18 K. Share, A. P. Cohn, R. Carter, B. Rogers and C. L. Pint, *ACS Nano*, 2016, **10**, 9738–9744.
19 Z. Xing, Y. Qi, Z. Jian and X. Ji, *ACS Appl. Mater. Interfaces*, 2017, **9**, 4343–4351.
20 S. Komaba, T. Hasegawa, M. Dahbi and K. Kubota, *Electrochem. Commun.*, 2015, **60**, 172–175.
21 Z. Jian, W. Luo and X. Ji, *J. Am. Chem. Soc.*, 2015, **137**, 11566–11569.
22 C. Chen, Z. Wang, B. Zhang, L. Miao, J. Cai, L. Peng, Y. Huang, J. Jiang, Y. Huang and L. Zhang, *Energy Storage Mater.*, 2017, **8**, 161–168.
23 R. Hao, H. Lan, C. Kuang, H. Wang and L. Guo, *Carbon*, 2018, **128**, 224–230.
24 D. Li, X. Ren, Q. Ai, Q. Sun, L. Zhu, Y. Liu, Z. Liang, R. Peng, P. Si and J. Lou, *Adv. Energy Mater.*, 2018, **8**, 1802386.
25 X. Wang, K. Han, D. Qin, Q. Li, C. Wang, C. Niu and L. Mai, *Nanoscale*, 2017, **9**, 18216–18222.
26 Z. Jian, S. Hwang, Z. Li, A. S. Hernandez, X. Wang, Z. Xing, D. Su and X. Ji, *Adv. Funct. Mater.*, 2017, **27**, 1700324.
27 G. Suo, J. Zhang, R. Li, Z. Ma, Y. Cheng and S. M. Ahmed, *Mater. Today Chem.*, 2023, **27**, 101300.
28 D. Li, J. Zhang, S. M. Ahmed, G. Suo, W. A. Wang, L. Feng, X. Hou, Y. Yang, X. Ye and L. Zhang, *J. Colloid Interface Sci.*, 2020, **574**, 174–181.
29 G. Suo, S. M. Ahmed, Y. Cheng, J. Zhang, Z. Li, X. Hou, Y. Yang, X. Ye, L. Feng and L. Zhang, *J. Colloid Interface Sci.*, 2022, **608**, 275–283.
30 R. Hao, Y. Yang, H. Wang, B. Jia, G. Ma, D. Yu, L. Guo and S. Yang, *Nano Energy*, 2018, **45**, 220–228.
31 D. Li, Y. Sun, S. Chen, J. Yao, Y. Zhang, Y. Xia and D. Yang, *ACS Appl. Mater. Interfaces*, 2018, **10**, 17175–17182.
32 Y. Li, R. A. Adams, A. Arora, V. G. Pol, A. M. Levine, R. J. Lee, K. Akato, A. K. Naskar and M. P. Paranthaman, *J. Electrochem. Soc.*, 2017, **164**, A1234.
33 X. Zhou, P. Wang, Y. Zhang, L. Wang, L. Zhang, L. Zhang, L. Xu and L. Liu, *J. Mater. Chem. A*, 2017, **5**, 12958–12968.
34 L. Jiang, L. Sheng and Z. Fan, *Sci. China Mater.*, 2017, **61**, 133–158.
35 K. Chaitra, R. Vinny, P. Sivaraman, N. Reddy, C. Hu, K. Venkatesh, C. Vivek, N. Nagaraju and N. Kathyayini, *J. Energy Chem.*, 2017, **26**, 56–62.
36 N. Sinan and E. Unur, *J. Energy Chem.*, 2017, **26**, 783–789.
37 G. Yuan, T. Wan, A. BaQais, Y. Mu, D. Cui, M. A. Amin, X. Li, B. B. Xu, X. Zhu and H. Algadi, *Carbon*, 2023, **212**, 118101.
38 J. Ruan, Z. Chang, H. Rong, T. S. Alomar, D. Zhu, N. AlMasoud, Y. Liao, R. Zhao, X. Zhao and Y. Li, *Carbon*, 2023, 118208.
39 A. Vijeata, G. R. Chaudhary, A. Umar and S. Chaudhary, *Eng. Sci.*, 2021, **15**, 197–209.
40 M. Kumari, G. R. Chaudhary, S. Chaudhary and A. Umar, *Eng. Sci.*, 2021, **17**, 101–112.
41 S. M. Ahmed, G. Suo, W. A. Wang, K. Xi and S. B. Iqbal, *J. Energy Chem.*, 2021, **62**, 307–337.
42 Q. Wang, C. Gao, W. Zhang, S. Luo, M. Zhou, Y. Liu, R. Liu, Y. Zhang, Z. Wang and A. Hao, *Electrochim. Acta*, 2019, **324**, 134902.
43 E. M. Lotfabad, J. Ding, K. Cui, A. Kohandehghan, W. P. Kalisvaart, M. Hazelton and D. Mitlin, *ACS Nano*, 2014, **8**, 7115–7129.
44 Z. Wu, L. Wang, J. Huang, J. Zou, S. Chen, H. Cheng, C. Jiang, P. Gao and X. Niu, *Electrochim. Acta*, 2019, **306**, 446–453.
45 G. Qi, Y. Liu, L. Chen, P. Xie, D. Pan, Z. Shi, B. Quan, Y. Zhong, C. Liu and R. Fan, *Adv. Compos. Hybrid Mater.*, 2021, **4**, 1226–1238.
46 M. Liu, H. Wu, Y. Wu, P. Xie, R. A. Pashameah, H. M. Abo-Dief, S. M. El-Bahy, Y. Wei, G. Li and W. Li, *Adv. Compos. Hybrid Mater.*, 2022, **5**, 2021–2030.
47 G. Fan, Z. Wang, H. Ren, Y. Liu and R. Fan, *Scr. Mater.*, 2021, **190**, 1–6.
48 G. Fan, Z. Wang, K. Sun, Y. Liu and R. Fan, *J. Mater. Sci. Technol.*, 2021, **61**, 125–131.
49 P. Xie, Z. Zhang, K. Liu, L. Qian, F. Dang, Y. Liu, R. Fan, X. Wang and S. Dou, *Carbon*, 2017, **125**, 1–8.
50 A. K. Chourasia, M. Shavez, K. M. Naik, C. Bongu and C. S. Sharma, *ACS Appl. Energy Mater.*, 2023, **6**, 378–386.
51 J. Yang, Z. Ju, Y. Jiang, Z. Xing, B. Xi, J. Feng and S. Xiong, *Adv. Mater.*, 2018, **30**, 1700104.

52 H. Fei, Y. Liu, Y. An, X. Xu, J. Zhang, B. Xi, S. Xiong and J. Feng, *J. Power Sources*, 2019, **433**, 226697.
53 D. Yoon, D. H. Kim, K. Y. Chung, W. Chang, S. M. Kim and J. Kim, *Carbon*, 2016, **98**, 213–220.
54 G. Dong, H. Wang, W. Liu, J. Shi, S. Sun, D. Li, H. Zhang, Y. Yang and Y. Cui, *ACS Appl. Energy Mater.*, 2018, **1**, 5636–5645.
55 N. Wang, Y. Wang, X. Xu, T. Liao, Y. Du, Z. Bai and S. Dou, *ACS Appl. Mater. Interfaces*, 2018, **10**, 9353–9361.
56 M. Kruk and M. Jaroniec, *Chem. Mater.*, 2001, **13**, 3169–3183.
57 J. Zhang, Z. Lyu, F. Zhang, L. Wang, P. Xiao, K. Yuan, M. Lai and W. Chen, *J. Mater. Chem. A*, 2016, **4**, 6350–6356.
58 L. Qie, W. Chen, H. Xu, X. Xiong, Y. Jiang, F. Zou, X. Hu, Y. Xin, Z. Zhang and Y. Huang, *Energy Environ. Sci.*, 2013, **6**, 2497–2504.
59 Q. Lu, B. Lu, M. Chen, X. Wang, T. Xing, M. Liu and X. Wang, *J. Power Sources*, 2018, **398**, 128–136.
60 H. Li, Z. Sun, L. Zhang, Y. Tian, G. Cui and S. Yan, *Colloids Surf., A*, 2016, **489**, 191–199.
61 Y. Xu, C. Zhang, M. Zhou, Q. Fu, C. Zhao, M. Wu and Y. Lei, *Nat. Commun.*, 2018, **9**, 1720.
62 E. Zhang, X. Jia, B. Wang, J. Wang, X. Yu and B. Lu, *Adv. Sci.*, 2020, **7**, 2000470.
63 J. H. Choi, G. D. Park and Y. C. Kang, *Chem. Eng. J.*, 2021, **408**, 127278.
64 J. Ruan, X. Wu, Y. Wang, S. Zheng, D. Sun, Y. Song and M. Chen, *J. Mater. Chem. A*, 2019, **7**, 19305–19315.
65 Z. Ju, S. Zhang, Z. Xing, Q. Zhuang, Y. Qiang and Y. Qian, *ACS Appl. Mater. Interfaces*, 2016, **8**, 20682–20690.
66 J. Ruan, F. Mo, Z. Chen, M. Liu, S. Zheng, R. Wu, F. Fang, Y. Song and D. Sun, *Adv. Energy Mater.*, 2020, **10**, 1904045.
67 W. Cao, E. Zhang, J. Wang, Z. Liu, J. Ge, X. Yu, H. Yang and B. Lu, *Electrochim. Acta*, 2019, **293**, 364–370.
68 C. Gao, Q. Wang, S. Luo, Z. Wang, Y. Zhang, Y. Liu, A. Hao and R. Guo, *J. Power Sources*, 2019, **415**, 165–171.
69 S. Tian, D. Guan, J. Lu, Y. Zhang, T. Liu, X. Zhao, C. Yang and J. Nan, *J. Power Sources*, 2020, **448**, 227572.
70 M. Liu, D. Jing, Y. Shi and Q. Zhuang, *J. Mater. Sci.: Mater. Electron.*, 2019, **30**, 8911–8919.
71 Z. Zhang, B. Jia, L. Liu, Y. Zhao, H. Wu, M. Qin, K. Han, W. A. Wang, K. Xi and L. Zhang, *ACS Nano*, 2019, **13**, 11363–11371.
72 Y. Sun, H. Xiao, H. Li, Y. He, Y. Zhang, Y. Hu, Z. Ju, Q. Zhuang and Y. Cui, *Chem. – Eur. J.*, 2019, **25**, 7359–7365.
73 H. Lindström, S. Södergren, A. Solbrand, H. Rensmo, J. Hjelm, A. Hagfeldt and S.-E. Lindquist, *J. Phys. Chem. B*, 1997, **101**, 7717–7722.
74 Y. Lei, L. Qin, R. Liu, K. C. Lau, Y. Wu, D. Zhai, B. Li and F. Kang, *ACS Appl. Energy Mater.*, 2018, **1**, 1828–1833.
75 Z. Wu, J. Zou, S. Shabanian, K. Golovin and J. Liu, *Chem. Eng. J.*, 2022, **427**, 130972.
76 H. D. Pham, K. Mahale, T. M. L. Hoang, S. G. Mundree, P. Gomez-Romero and D. P. Dubal, *ACS Appl. Mater. Interfaces*, 2020, **12**, 48518–48525.
77 M. Moussa, S. A. Al-Bataineh, D. Losic and D. P. Dubal, *Appl. Mater. Today*, 2019, **16**, 425.
78 S. Dong, Z. Li, Z. Xing, X. Wu, X. Ji and X. Zhang, *ACS Appl. Mater. Interfaces*, 2018, **10**, 15542.
79 F. Ming, H. Liang, W. Zhang, J. Ming, Y. Lei, A.-H. Emwas and H. N. Alshareef, *Nano Energy*, 2019, **62**, 853.
80 H. D. Pham, J. F. Fernando, M. Horn, J. MacLeod, N. Motta, W. O. Doherty, A. Payne, A. K. Nanjundan, D. Golberg and D. Dubal, *Electrochim. Acta*, 2021, **389**, 138717.